SAND2017-1719J

Noname manuscript No.
(will be inserted by the editor)

Integrated proximity, contact and force sensing using elastomer-embedded commodity proximity sensors

Radhen Patel · Rebecca Cox · Nikolaus Correll

Received: date / Accepted: date

Abstract We describe a combined proximity, contact and force (PCF) sensor based on a commodity infrared distance sensor embedded in a transparent elastomer with applications in robotic manipulation. Prior to contact, the sensor works as a distance sensor (0–6 cm), whereas after contact the material doubles as a spring, with force proportional to the compression of the elastomer (0–5 N). We describe its principle of operation and design parameters, including polymer thickness, mixing ratio, and emitter current, and show that the sensor response has an inflection point at contact that is independent of an object's surface properties, making it a robust detector for contact events. We then demonstrate how arrays of sensors, custom made for a standard Baxter gripper as well as embedded in the finger of the Kinova hand, can be used to (1) improve gripper alignment during grasping, (2) determine contact points with objects, (3) obtain simple 3D models using both proximity and touch, and (4) register point clouds from touch and RGB-D data.

Keywords Robotic Grasping · Manipulation · Dynamic force sensing · PCF-sensor

1 Introduction

Grasping and manipulation remain hard challenges in robotics. After identifying an object's pose, the robot's end-effector needs to be controlled to create a sufficient number of constraints for successful pick-up while maintaining the object's pose until all desired contact points are reached, thereby preventing the object from moving out of the end-effector's reach. The ability to use in-hand sensing to better align with an object and stop exerting forces once contact is made, might allow to provide these constraints without affecting the object's pose. Dollar et al (2010) use touch sensors to determine whether a grasp is successful, but the sensors cannot be used to improve the grasp prior to contact. An alternative to sensing is to use environmental constraints. For example, pushing an object against a wall (Dafle et al, 2014) or picking objects out of a bowl (Deimel and Brock, 2014) reduces uncertainty in object pose, which has been shown to increase grasping and re-grasping success without relying on any in-hand sensing. Planning such motions requires precise knowledge of the environment's geometry, however, and also such strategies are likely to benefit from active sensing to determine whether an object has reached a desired pose.

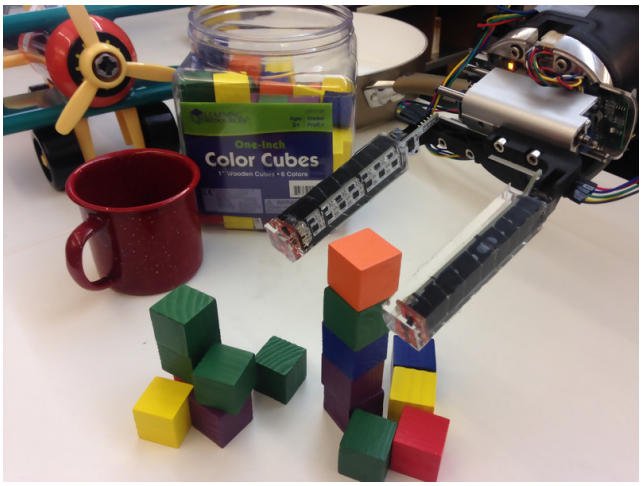

Fig. 1: PCF-sensors on a Baxter parallel gripper. Seven infrared sensors are spaced along each finger's contact area, and one is mounted at each tip for object detection and force control

R. Patel, R. Cox and N. Correll
University of Colorado Boulder
E-mail: ncorrell@colorado.edu

Yet, in commercially successful systems, that are widely deployed, in-hand sensors are virtually non-existing as they are difficult to manufacture and expensive. At the same time, the algorithmic foundations for reactive grasp planning are only sparsely developed, with most of the focus on the sense-plan-act model that requires precise sensing and actuation. This has been nicely illustrated at the 2015 Amazon Picking Challenge, where only one out of 25 teams used tactile feedback for contact sensing (Correll et al, 2016).

Motivated by this apparent gap both in available hardware and applications for in-hand sensing, we present a simple and low-cost dynamic tactile sensor that combines proximity, contact and force (PCF). The proposed PCF-sensor is simple to manufacture and easy to integrate with existing hardware. The PCF-sensor consists of a commodity digital infrared distance sensor that is embedded in a soft polymer, which doubles as a spring for force measurements based on Hooke's law. We demonstrate how the discontinuity that the elastomer coating introduces into the sensor response can be exploited to detect contact independently of surface reflectivity. After describing other sensors that are closest to the work presented here in Sec. 1.1, we explain the sensor's manufacturing and principle of operation in Sec. 2. The impact of various design parameters is shown in Sec. 3, and calibration results are shown in Sec. 4. We then demonstrate how the sensor can support a robot during grasping and manipulation in 5.

1.1 Related work

Tactile sensing is widely considered an essential capability for efficient grasping and manipulation (Dahiya et al, 2010). By touching an object, it is possible to measure contact properties such as contact forces, contact position, and possibly even gather information about an object's surface properties. Apart from the sensing capabilities the sensors need to be rugged enough to withstand chemical and mechanical abrasion. Various types of tactile sensors based on various transduction methods namely, strain gauges, resistive/piezoresistive, capacitive, Tunnel effect, ultrasonic, impedance, mechanical, piezoelectric and magnetic effects have been reviewed by Dahiya et al (2010).

Wang and Beebe (2002) report a silicon piezoresistive sensor measuring both compressive and shear forces at the skin-object interface. Piezoresistive touch sensors are made of materials whose resistance changes with the applied force/pressure. Zhu and Spronck (1992) developed a capacitive tactile sensor with a resolution of 0.05 N over the range of 10 N for forces in both normal and tangential directions. A soft tactile sensor, comprising multiple capacitors embedded in polydimethylsiloxane (PDMS), was reported with a minimum detectable force of 10 mN by Lee et al (2008). Since capacitive sensors can be made very small they allow construction of dense sensor arrays. Gray and Fearing (1996) developed an 8X8 capacitive tactile sensing array of 1 mm^2 area with a spatial resolution exceeding that of a human by a factor ten. Although touch sensors based on capacitive mode of transduction are very sensitive, stray capacity and severe hysteresis are their major drawbacks.

Optical sensors use the change in light intensity to measure pressure. Fiber Bragg gratings based sensors enable small size and high sensitivity. Zhang et al (2013) embed a soft fiber optic sensor based on polymer fiber Bragg gratings into a soft PDMS film for simultaneous measurement of shear and normal stresses. A fiber optical sensor for a multi-fingered robotic hand was designed by Jiang et al (2015) for contact force and contact location sensing. Since optical fibers are flexible, they can be spanned out to make large area skin pressure sensors as illustrated by Ohmura et al (2006).

Strain sensors based on Gallium-Indium alloys Chossat et al (2013) have been embedded into soft robotic fingers to measure curvature and — in conjunction with air pressure — to detect the presence of objects (Farrow and Correll, 2015) and to adjust a grasp if necessary (Farrow et al, 2016).

Hughes and Correll (2015) use microphones to measure vibrations/noise at the onset of an object hitting a surface to identify textures. Similarly, Ando and Shinoda (1995); Nakamura and Shinoda (2001) use ultrasound to detect contact events and slip. How to use all of this tactile information during control is a topic of ongoing research (Dahiya et al, 2013; Bohg et al, 2014).

Part of the challenges with manufacturing and signal processing that all of the above sensors share to some extent, can be countered by using commodity digital sensors. For instance, Tenzer et al (2014) cover barometric pressure sensors with flexible polymers to provide contact and pressure sensing. Similarly, Konstantinova et al (2015) have integrated optical proximity sensors into deformable rubber domes or urethane foam (Hellard and Russell (2002); Rossiter and Mukai (2006); Fujimori et al (2009)), which both alter light reflection upon compression and shear, a phenomenon known as frustrated reflection. Finally, Lancaster (2004) combines off-the-shelf proximity sensors embedded in elastomers with capacitive sensing to perform directional force sensing.

Using distance sensors within robotic hands (Balek and Kelley, 1985; Hsiao et al, 2009) or skin (Mittendorfer and Cheng, 2011) is attractive to improve a grasp

during the approach phase. Hsiao et al (2009) integrate optical proximity sensors inside the fingertips of a Barrett Hand in order to perform reactive online grasping. Maldonado et al (2012), equips the fingertips of robot manipulator TUM-Rosie with proximity sensors to measure the distance to objects.

There also exist approaches that use both distance and force simultaneously. Goger et al (2013) and Farrow et al (2017) use capacitive sensors to measure proximity of (conductive) objects as well as pressure after contact. Mittendorfer et al (2015) combine optical proximity and capacitive pressure sensing to realize a multimodal tactile sensing skin. In this paper, we demonstrate how both distance and force along with dynamic tactile sensing can be achieved using a single off-the-shelf infrared sensor, allowing for making the device small enough for finger-tip operation, simple to manufacture, and low-cost, while providing performance that is comparable to the above approaches. This paper is an extended version of (Patel and Correll, 2016) and contains additional results presented by Patel et al (2016) and Cox and Correll (2017), providing a comprehensive summary of the proposed sensor and its applications.

2 Sensor design

The key idea of the proposed PCF-sensor is to use infrared proximity sensing to measure the distance to an object through a transparent polymer and to measure the force an objects exerts by measuring the compression of the polymer. Infrared sensors are strongly nonlinear and highly dependent on the surface properties of the sensed objects and the angle of incidence. They are sensitive to cross-talk from other sensors or infrared light in the environment. Increasing use in consumer electronics such as smart phones has led to a new generation of infrared sensors that improve cross-sensitivity by integrating sensor and emitter with digital signal processing.

We have chosen an integrated proximity and ambient light sensor VCNL 4010 (Vishay Semiconductors). This device has a miniature $3.95 \times 3.95 \times 0.75\ mm^3$ package which combines an infrared emitter and PIN photodiode for proximity measurement, ambient light sensor, a signal processing IC, a 16 bit ADC, and inter-integrated-circuit (I^2C) communication interface while requiring only very few external components (four filter capacitors). The chip allows setting a large variety of parameters, the most important being the emitter current (20mA to 200mA in increments of 10mA), and the carrier frequency in the range from 390.625 kHz–3.125 MHz in four increments. The ability to select the frequency of each sensor enables arranging sensors in opposite pairs, such as required on a robotic gripper, without interference. The emitter current should not be confused with the actual power consumption, which is less than 4 mA when performing 250 measurements per second at full (200 mA) power, and in the order of μA when doing 10 or less measurements per second.

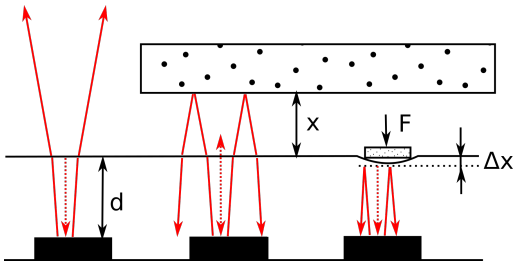

Fig. 2: Schematic sensor design illustrating key quantities. Infrared lobes are reflected at the interface of PDMS/air due to Fresnel reflection, as well as from close-by objects. Forces lead to deformation of the PDMS that reduces its width d by Δx.

We coupled multiple such integrated proximity and ambient light sensors using an I^2C multiplexer (TCA9548A, Texas Instrument). This chip has a programmable 3-bit address, which permits to create arrays of up to 8×8 sensors. At 100 kHz I^2C bus frequency, a single measurement requires 1470 μs including communication, allowing to read a 8×8 array at 20 Hz and a strip of eight such sensors at 85 Hz.

To enable force measurements, the infrared sensors are embedded in a thin layer of PDMS (Dow Corning Sylgard 184), see also Figure 2. PDMS is a widely used silicon elastomer, whose mechanical and optical properties have been widely studied (Cai et al, 2010, 2013; Chen et al, 2006). It is simple to manufacture and cheap, while providing good transparency and mechanical properties such as resistance to chemical and mechanical abrasion.

2.1 Principle of operation

As the infrared light (890nm) from the emitter passes through a thin layer of PDMS, it is reflected by nearby objects and received by the photo-receiver. The amplitude and phase of the light vary as a function of the distance to the surface, its orientation, color and texture. The net reflected intensity received is approximately the inverse of the square of the distance.

Due to the quadratic decay of light amplitude with distance, the sensor has its highest resolution right after its minimum range of 0.5mm. It is therefore possible to measure small variations in elastomer thickness in the order of hundredths of millimeters. We exploit this effect by measuring the elastic deformation that occurs

when an object is pressed against the sensor. As the elastomer can be approximated by a spring with a constant Young's modulus E (for light pressure), the force is given by

$$F \approx \frac{EA}{d}\Delta x \tag{1}$$

with A the contact area over the sensor, d the width of the PDMS layer and Δx the measured deformation. Note that the sensor area is constant and smaller than the actual contact area of typical objects. Yet, the value of F is approximate as PDMS cannot be infinitely compressed and eventually changes its density and thereby absorption properties. A brief formulation of the nature of infrared light in PDMS is as follows.

Let the emitted light intensity be I_0 and the measured reflected intensity from an object be I. Let the thickness of the rubber be d and the distance to the object x, see also Figure 2. Depending on the index of refraction of the rubber material, a fraction R of the light will be reflected from the interface between rubber and air, a fraction κ will be scattered, and a fraction α will be reflected at the target surface. Assuming that the light intensity decays quadratically with distance, we can approximate the amount of returned infrared as

$$I_{x>0} \approx I_0(1-R)\frac{\alpha}{(d+x)^2} + I_0 R\frac{1}{d^2} - \kappa I_0. \tag{2}$$

The reflection at the PDMS/air interface can be calculated using the Fresnel equation Born and Wolf (1999), which reduces to

$$R = \left|\frac{n_1 - n_2}{n_1 + n_2}\right|^2 \tag{3}$$

for normal incidence. With the refractive index of PDMS $n_1 \approx 1.41$ and that of air $n_2 \approx 1$, around 2.9% of the light gets reflected from the internal surface of the PDMS as well as on the outside on the return path.

This formalism helps us to better understand certain edge cases. First, when $d \ll x$, the light intensity at the receiver is dominated by $\frac{I_0 R}{d^2}$, which leads to saturation of the sensor, if I_0 is too large or d is too small. The width d of the PDMS therefore governs the maximum current at which we can operate the sensor and thereby the maximum attainable range. At the same time, the width governs the maximum allowable Δx and thereby the maximum force and its resolution that the sensor can measure.

Once the object touches the sensor surface, i.e. $x = 0$, (2) reduces to a constant, which is only a function of material properties. After touching, the PDMS gets compressed by $\Delta x \approx \frac{dF}{EA}$, leading to

$$I_{x<0} \approx I_0\frac{\alpha}{(d-\frac{dF}{EA})^2} - \kappa I_0 \tag{4}$$

Note that (4) still depends on the surface reflectance α, which therefore needs to be known for accurate force measurements. we observe, however, that $x = F = 0$ is an inflection point of the signal that can be potentially detected in the sensor's response and therefore allows us to detect contact independently of surface properties. Indeed, equations (2) and (4) yield the same values for $x = 0$ and $F = 0$, respectively, but have different slopes.

We note that compression of the PDMS eventually alters the scattering and absorption properties, which dramatically increase for certain high pressures. This effect is dependent on a variety of properties including the chemical composition, impurities and sensor geometry, and is beyond the scope of this paper.

2.2 Manufacturing

We designed PCF-sensor arrays for the parallel grippers of the Baxter robot from Rethink Robotics and for the fingers of the Jaco arm from Kinova Robotics. The size of the sensor printed circuit boards before PCB embedding for the Baxter robot (Figure 1) is $111 \times 10 \times 2$ mm and that on the Kinova hand (Figure 5) is $20 \times 11 \times 0.7$ mm in size. We manufactured two separate pairs of sensor for gripper with grasp ranges varying from 0-68 mm to 68-144 mm for the Baxter robot. Each sensor is an array of eight infrared sensors, seven on each of the parallel sides and one on each fingertip. The senors on the fingers of the Kinova hand consists of an array of two infrared sensors, both close to the anterior side of the fingertip.

The infrared sensors requires few external components (3 capacitors). This allows us to pack multiple such infrared sensors tightly in compact spaces, e.g., the finger tips of a Kinova hand, while maintaining the original form factor of the mechanism. The sensor is covered with a layer of PDMS by placing it in a custom mold. The mold for the Baxter fingers is made from acrylic sheets, whereas the mold for the Kinova fingers required 3D printing. After placing the structural elements and the PCB into the mold, we pour two-component liquid polymer (PDMS) into the mold. This process is illustrated in Figures 3 and 4. In order to avoid air bubbles at the interface between PDMS and the sensor, we degas the liquid polymer in a vacuum chamber before pouring it into the mold. We use painter's tape to ensure that the PDMS does not leak out. The PDMS is then cured in an oven (Quincy Lab)

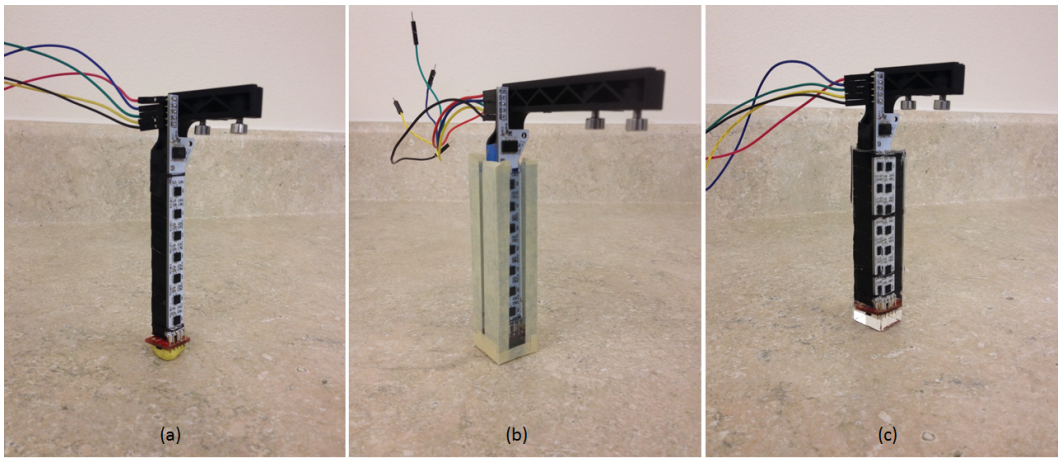

Fig. 3: (a) Sensors are mounted on the parallel gripper, (b) placed in an acrylic mold, filled with PDMS and (c) cured.

at 70^oC for 20 minutes. This forms a robust and compliant rubber contact surface for grasping and manipulation. To improve repeatability of the optical properties of amorphous PDMS, it is advised to purify the raw materials before the mixing process to avoid extrinsic losses, e.g., by particle scattering. The base material and coupling agents should thus be filtered using a mixed cellulose ester membrane filter of pore size of 0.2 μm. The entire process takes around 5 hours to prepare a pair of these sensors. Note that the curing time depends greatly on the amount of liquid polymer and on the mold material. The above mentioned values are experimentally reached for the amount of PDMS required to cover a standard Baxter parallel gripper in an acrylic mold of 5 mm thickness.

The final products, a parallel gripper for the "Baxter" robot and the "Jaco" arm from Kinova Robotics are shown in Figure 1 and 5, respectively.

2.3 System integration

The infrared sensors are multiplexed onto a single I^2C channel, which is interfaced to an Arduino microcontroller. The microcontroller periodically reads all sensor values and outputs them to a serial line, which connects to a host computer via USB. A ROS node retrieves the data and makes it available to the rest of the system. Integration of the sensor data with perception for control is described in more detail in Patel et al (2016) (Baxter robot) and Patel et al (2017) (Kinova robot). All software is available open-source at `https://github.com/correlllab/cu-perception-manipulation-stack`.

3 Design parameters

To experimentally characterize the performance of the proposed tactile sensor, we first characterized the response of an individual sensor and then the sensing capabilities of a complete array by installing it on a parallel gripper. Figure 6 shows the experimental setup to test and characterize the performance of these sensors. For having consistency in the experimental analysis, the calibration rig is designed in a way which allows the testing of both, an individual sensor and a complete array in their proximity and force regimes. The setup consists of a $0.15 \times 0.13\ m^2$ screen that is mounted vertically on a sliding rod with a precise linear control. A digital force gauge (Shimpo FGV-10XY) is mounted horizontally on the opposite side of the screen to measure the force exerted on the sensor.

Considering the air-PDMS surface as the screen's zero position, the screen is moved in discrete steps towards the sensor to measure distance. After the screen touches the surface of the PDMS, the screen is rigidly fixed at a place where the force gauge reads 1N. A total of five readings are then taken at intervals of 1N by further compressing the screen upon the sensor. Note that this approach allows us to seamlessly measure both distance and force as well as experimentally detect contact, which is defined by the force sensor changing from zero Newton to a positive value.

We have been using this setup to study the effects of various fabrication parameters, particularly the thickness of the PDMS film, mixing ratio of base to curing agent of pre-polymer and the operating sensor current value on the sensors response.

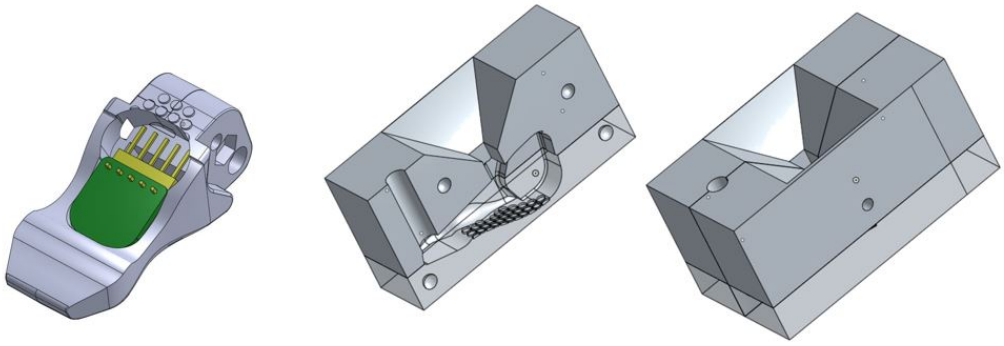

Fig. 4: Left: A modified finger for the Kinova hand with a cut-out for a small PCB. The finger consists of two parts that are held together with a M3 screw, which allows mounting it onto the tendon of the Kinova hand. Middle: The left side of a four part mold that can hold a 3D printed finger. A funnel facilitates pouring PDMS, an air-duct allows air to escape, and four half-spheres protruding from the other half of the mold facilitates alignment. Right: Complete mold.

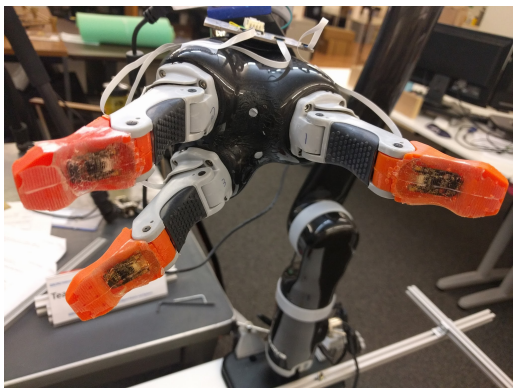

Fig. 5: PCF-sensor for the Kinova Jaco robot arm with an array of two infrared sensors per finger.

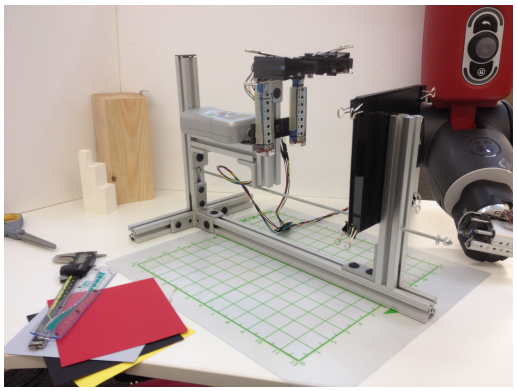

Fig. 6: Experimental setup to conduct proximity and force measurements.

3.1 Current

We recorded single-point measurements at distances from 0 to 6cm in increments of 1cm, as well as force from 0N (0cm) to 5N in increments of 1N for current values from 40mA to 200mA in increments of 40mA (Figure 7). PDMS with mixing ratio 8:1 has been applied to a thickness of 6mm above the sensor. Results show saturation of the sensor for distances below 1cm at current values exceeding 80mA due to Fresnel reflection inside the PDMS. At 80mA, the sensor saturates at less than 2N force, whereas a 40mA setting allows to measure across the range from 0 to 5N. Changing the current therefore allows trading range for resolution. At 80mA, distances from 0 to 6 cm result to ADC values from 5086 to 45789, or 40703 distinct values. At 40mA, the same range results in only distinct 20245 values, corresponding to a reduction of resolution from 2.96μm to 1.47μm. While not relevant at longer distances given the accuracy of the sensor being four orders of magnitude worse than its resolution, reducing the current extends the sensor's range from around 2N to 5N at an ADC resolution of 80μN and 285μN, respectively.

3.2 Thickness

The thickness of PDMS has a considerable effect on the amount of light absorbed and scattered within the material. (The amount of light reflected back from the air-PDMS surface does not change as it depends only on the refractive indexes of the material.) Figure 7, middle, shows the response of two sensors cast in PDMS with the base to curing agent in a 8:1 ratio and for thicknesses of 6mm and 12mm. Considering distance measurements from 0 to 6cm, absorption within the material compresses the range of raw ADC values from $[5084; 48201]$ for 6mm PDMS coating to $[3956; 25612]$ for 12mm PDMS coating, thereby reducing the resolution of the sensor for the 0–6cm range from 1.39μm to 2.77μm. This effect is more accentuated in the force domain where the ADC values for measurements from 0

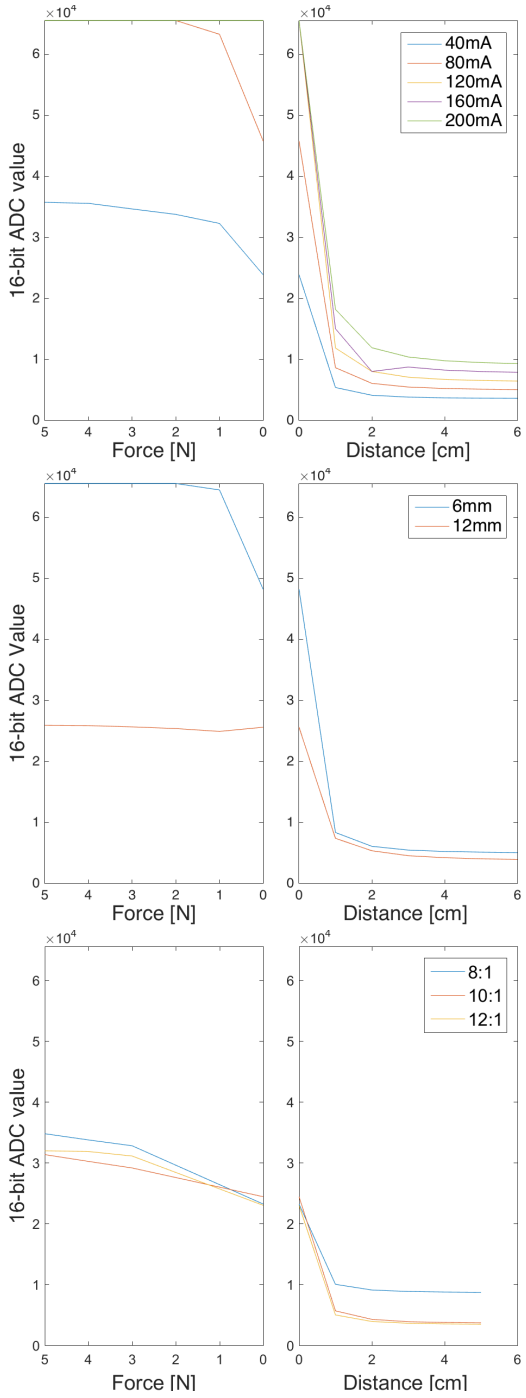

Fig. 7: Design parameters of the sensor. Top: Sensor response for different current settings. Middle: Sensor readings as a function of PDMS thickness at 80mA. Bottom: Sensor readings as a function of mixing ratio of the two PDMS components.

to 1N range from 48454 to 64824 (16370 individual values or approximately $60\mu N$ resolution) for 6mm PDMS coating, but span only a range of approximately 1000 values for the entire range of 0 to 5N for 12mm PDMS coating. For thicker coatings, we also observe a systematic non-monoticity of the signal for small forces, which is consistent for different current values and surface reflectance, and whose origin we currently cannot explain and which we wish to study in further work.

3.3 Mixing Ratio

Chen et al (2006) use Fourier Transform Infrared Spectrometry to characterize the mid-infrared transmission of thin PDMS film. The transmittance of infrared light is found to depend strongly on the mixing ratio of base and curing agents causing the composition of PDMS to change; lower mixing ratios results in higher transmittance. Maximum transmittance of about 95% is found between wavenumbers 2490-2231 cm^{-1} with mixing ratios of 8:1. To compare the results at wavenumbers 12500-10526 cm^{-1} (800-950 nm), we prepared three mixtures of PDMS with different mixing ratio of the base and curing agent (5:1, 10:1, and 12:1). Figure 7 shows the sensor proximity and force values for different mixing ratios. Albeit the Young's modulus of PDMS changes by about 35-40% while the density changes by only 1% over the range of mixing ratio from 8:1 to 12:1 (Armani et al, 1999), there is only little difference in the force region among these values, but distance measurements are more distinct, in particular for 8:1 mixing ratios. As the cross-over from distance to force is at approximately the same sensor reading, we deduct that 8:1 mixing ratios provide the widest dynamic range in the force regime, but the smallest dynamic range in the distance regime.

4 Calibration

For calibrating the relationship between sensor reading and actual distance, we first characterize the sensitivity of the sensor to surface reflectance, and then record data for different distances across a variety of sensors for white paper. We have chosen a width of 6mm at a mixing rate of 8:1 for the remainder of this paper due to the higher dynamic range in the distance and force regime, respectively.

4.1 Color

The intensity of light reflected from objects are greatly dependent on the color, pose and surface properties of the object. We chose five different colored target objects (red, yellow, white, gray and black, Canson, 150 gsm) as described in Benet et al (2002). The colored cardboard papers were mounted on the screen shown in Figure

6 which served as target objects for a distance sensor coated by 6mm PDMS at 8:1 mixing ratio.

Figure 8 shows the response of the sensor to different colors. The proximity measurements are comparatively lesser influenced by the reflective properties of the target surface than the force measurements. Albeit bright colored materials give better readings than darker ones, there is not any significant difference in the sensor response to different colors, except for the black paper.

These findings are in line with Benet et al (2002), who calculate the reflectance for a variety of colors to be in the range of 0.9 (gray) to 1.0 (white), whereas black cardboard has a reflectance of 0.12. Cardboard of all colors is much more reflecting than wood (0.77), brick (0.61) or concrete (0.53), but much less reflecting than specular surfaces such as polished plastic or china.

4.2 Distance

In order to obtain a relationship between sensor readings and actual distance we recorded data from 14 different sensors and white paper. We arranged seven sensors in a line at 10mm spacing. We recorded the response of two such arrays (14 sensors) at 24 distances ranging from 0.5 to 19cm and 50 measurements each for 120mA. Albeit 120mA leads to saturation in the force regime (when using white paper), this value allows us to obtain better ranging and works fine with objects that are less reflecting. The data is shown in Figure 9.

We fitted this data with a function of the form $y = ax^b + c$ using MATLAB's curve fitting toolbox's trust-region method and bisquare weighting of outliers. The candidate function corresponds to physical intuition (with $b = -2$) and can be inverted to

$$x = \frac{1}{((y-c)/a)^{\frac{1}{b}}} \tag{5}$$

Notice that the denominator of the above equation includes the b-th root, which yields complex values for $y < c$. This happens whenever a sensor reading falls below the assymptote of the fitted curve, which is often the case for farther-away measurements. We therefore convert all measurements into decibel scale using $\log_{10} \frac{I}{I_\infty}$, where I_∞ is the measurement obtained in plein air. With $b \approx -1$ after fitting on the log-scale, all distance measurements remain real. The fit as well as absolute error for both the raw and PDMS-coated sensors are shown in Figure 9, middle. As expected, we observe a slightly higher absolute error for all measurements with PDMS, which initially makes objects appear closer (up to about 7cm) and then farther apart than the raw sensor. Data follows a similar trend for distances from 10 cm to 19 cm, but are not shown as the high error at this range makes those measurements impractical to use.

4.3 Force

As force measurements are much more susceptible to surface reflectance, we have performed fits for a variety of colored papers using data from Figure 8, left. Results for a subset (white, red, black) are shown in Figure 8, right. Using an equation of the form $y = ax^b$ has provided good results, with R-squared values ranging from 0.9898 (black) to 0.9953 (white).

5 Applications

In this section we show how proximity, contact and force information can be used in a grasping and manipulation context. We first demonstrate using proximity information from the PCF-sensors to center the gripper around an object to improve grasping. We then shown how contact information can be used to determine when and where on a gripper an object is touched, which is important during manipulation. We then demonstrate how proximity and contact information can be used to create simple 3D models of a series of objects, and how this information can be used to register point cloud information from tactile and RGB-D sources. Unless otherwise noted, all objects are chosen from the Yale-CMU-Berkeley (YCB) Object and Model set (Calli et al, 2015).

5.1 Gripper centering

We investigate proximity sensing to center a gripper around an object. This is important when successful grasping requires both fingers to simultaneously make contact. For example grasping a cup at its handle induces a turning motion that needs to be counteracted by the opposite finger before the cup has turned out of the robot's grasp. Similarly, removing a block from a Jenga tower (Kröger et al, 2008) requires to create force-closure with the block while inducing a minimum amount of motion on the block itself.

Figure 10 depicts a similar situation, in which imprecise alignment will collapse a tower of wooden blocks. The grippers were deliberately misaligned and closed in discrete steps and the response form the sensor was recorded. The response from the sensors on the right

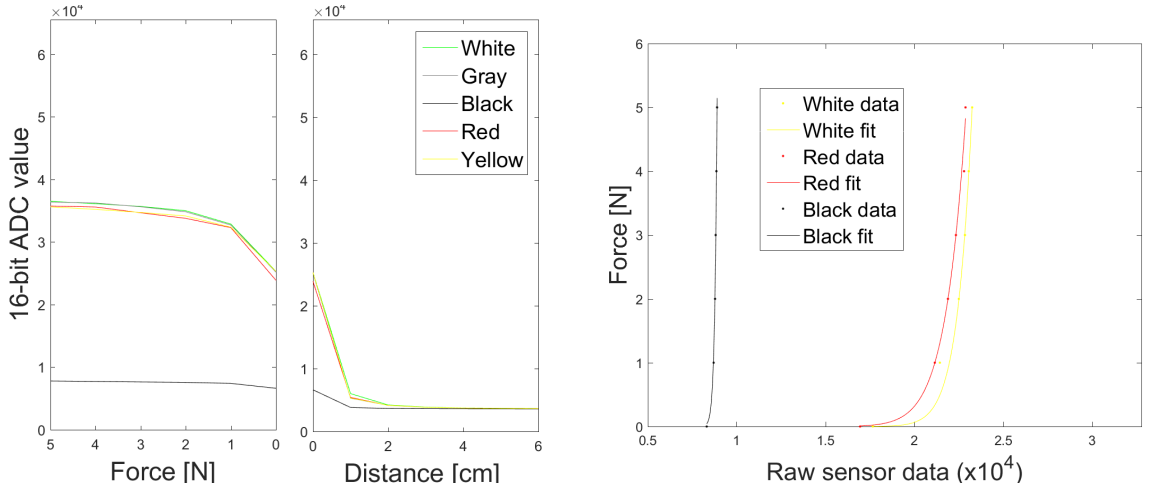

Fig. 8: Left: Sensor response (PDMS 6mm, 8:1 mixing ratio) to different color targets. Right: Raw sensor readings vs. actual force for different colors and fit of the form $y = ax^b$.

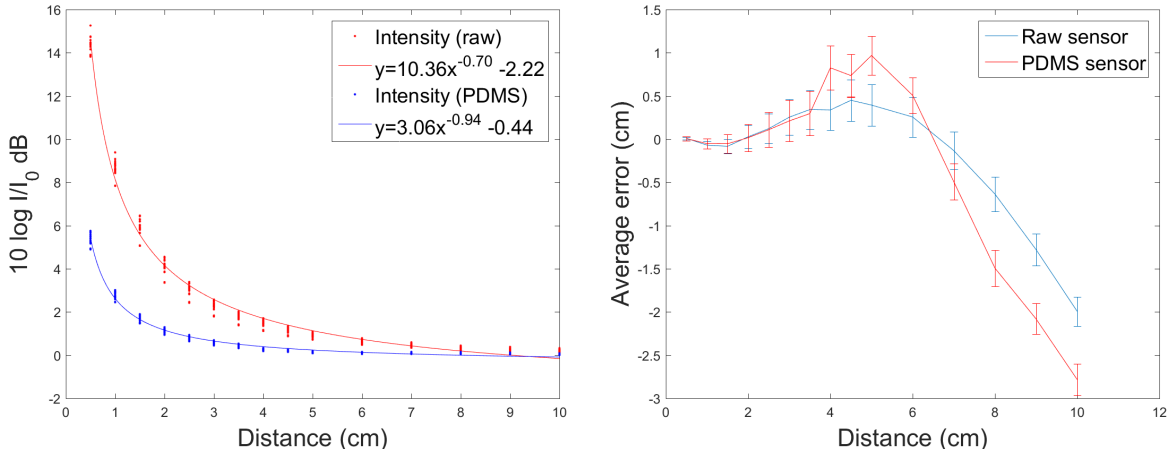

Fig. 9: Left: Sensor response to different distances at 120mA. Without PDMS (raw) and covered with 6mm PDMS with 8:1 mixing ratio averaged over 14 different sensors.

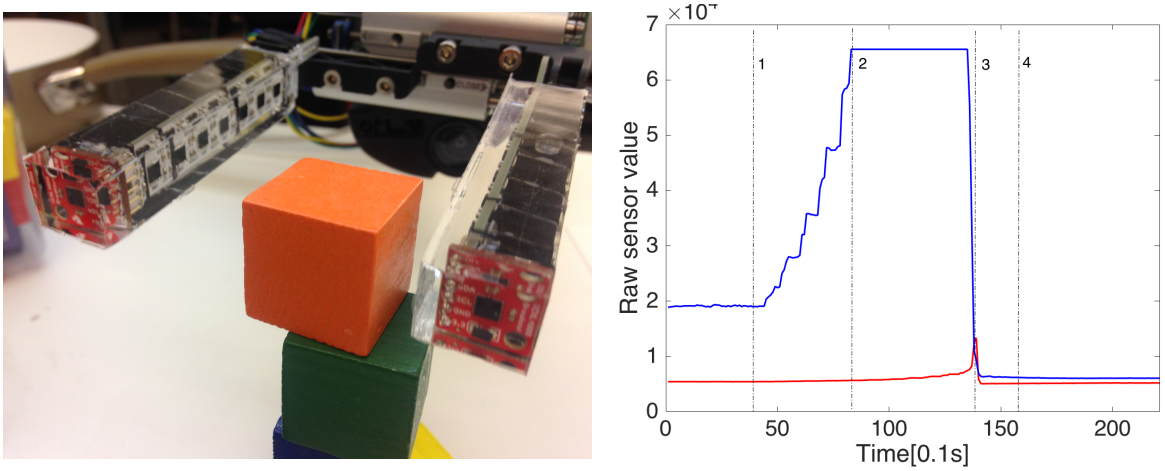

Fig. 10: Deconstructing a tower of 1-inch cubes requires exact centering of the gripper in order to prevent the cubes from falling. The plot to the right shows raw sensing values for the left (blue) and right (red) finger. The left gripper approaches the cube in phase 1–2. It makes contact at 2 while the right finger continues its approach during 2–3. As the left gripper is still pushing the cube, it will eventually fall of the green cube and disappears from both grippers' field of view (3–4).

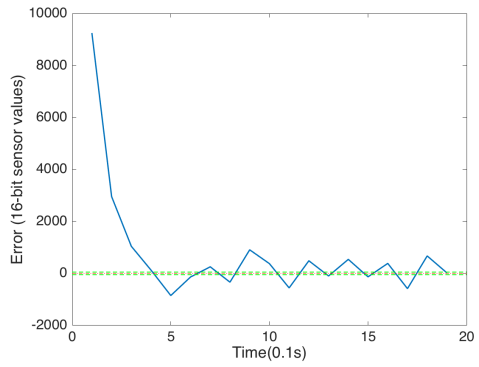

Fig. 11: Using the average of differences in sensor readings measured from the left and right finger (Figure 10) to center an object.

finger is shown in blue and the response from the left finger is shown in red.

Assuming the surface properties (reflectance) are the same on both sides of the object, data shown in Figure 10 can be used to servo the end-effector to a position, in which both distances are roughly equal using simple feedback control and inverse kinematics (Baxter SDK PyKDL), see Figure 11.

5.2 Contact point evaluation

Figure 12, middle, shows the raw measurements of all sensors when grasping the handle of the YCB pan (Figure 12, left). The data clearly shows the fingers approaching the handle. Closer inspection of contact data, here the 5th sensor of the right finger, reveals that gentle pressure drives the sensor to roughly 2×10^4 (Figure 12, middle), which is similar to values generated by contact with black card-board (Figure 12, right). Furthermore, fitting a spline to the raw data and calculating its derivative (MATLAB `spline` and `fnder`), reveals that the sensor response has an inflection point close to where the black cardboard crosses from the distance to the force regime. Performing the same operation on data from the left finger suggests a material of slightly higher reflectance (the sensor maxes out at 2.4×10^4) with a cross-over point at a raw value of 17529. Indeed, we are able to correctly detect the cross over point for all experiments shown in Figure 8 (five different colors), left, for currents ranging from 40 mA to 200 mA in increments of 40 mA (25 experiments).

5.3 Object and Touch detection

A different perspective on contact evaluation is provided from the study of dynamic sensing in the human fingertip. Following Romano et al (2011), we pass the raw sensor input through a high-pass filter to detect contact events, which appear as extrema in the high-pass signal. The resulting signals are roughly equivalent to the SA-I and FA-I signals in the human hand Romano et al (2011), that is constant pressure and dynamic tactile events. A signal similar to SA-I estimate of the total fingertip force can be obtained by summing all the sensors values on each finger:

$$F_l(t) = \sum_{i=1}^{7} f_i(t). \tag{6}$$

Similarly, to obtain a signal similar to FA-I channel we use a discrete-time first order Butterworth high-pass filter with a cut-off frequency of 5 Hz for a 20 Hz sampling rate of the sensor:

$$\tilde{F}(t) = \sum_{i=1}^{14} h_f(t) * f_i(t). \tag{7}$$

After calibrating the sensors (subtracting the average of the base values over time t) moments before executing the grasp, values ranging above and below specific thresholds are considered object and contact detection events respectively (Figure 13). The gradual increase in the SA-I channel refers to an object detection event, but shows as a peak in the FA-I channel, indicating a contact event. A flat top in the SA-I channel is short moment when an object is in contact with the sensors. A drop in the SA-I channel indicates the object separating from a finger, showing as a negative peak in the FA-I channel, indicating a release event.

We note that the FA-I signal is independent of the surface properties *and* the force an object exerts, and has been reliably reproduced by touching almost all objects in the YCB dataset as well as a feather landing on it[1].

5.4 3D Sensing

As the end-effector position of a robot is usually well known, proximity and contact data can also be used to construct simple 3D models. Using an array of sensors, we combine proximity measurements obtained from scanning an object such as a cup to form a crude 3D model of the object as shown in Figure 14. The robot wrist joint is rotated around the object in increments of 0.17rad in the interval of $[-\pi; \pi]$. Using the actual encoder values of the Baxter robot at each step and converting sensor readings into centimeters using (5) yields polar coordinates of each point where the infrared light hits the

[1] `https://www.youtube.com/watch?v=QMzcKJtNkxA`

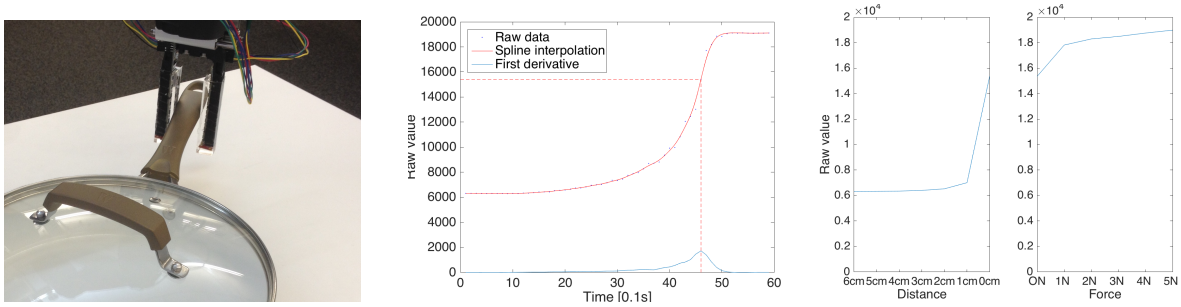

Fig. 12: Left: Baxter gripper augmented with finger sensors trying to infer object properties. Middle: Close-up on sensor 5 of the right finger and its numerical derivative. Horizontal and vertical lines indicate the raw value that corresponds to the derivative's peak. Right: Calibration data for black cardboard. Horizontal and vertical lines indicate the raw value that corresponds to crossing from distance to force.

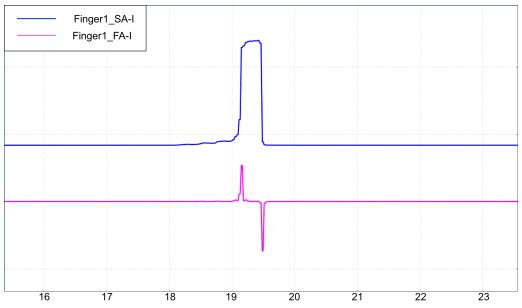

Fig. 13: Sensor response (analog reading) from the SA-I (blue) and FA-I (pink) channel versus time(s) to a spoon handle when brought close to, touched and separated from the PCF-sensors on the finger of Jaco arm.

object. Albeit noisy due to non-orthogonal incidence angles at the handle and the bottom of the cup, the fidelity of the model is sufficient to highlight the presence of the cup's handle and is, after removing outliers, close ($\pm 0.5cm$) to the cup's true diameter.

We also selected a toy airplane form the YCB object set which has a specular surface. Figure 15 shows the proximity sensors being swept across the wing to detect a possible grasp location, this time using a horizontal motion.

Figure 15, right, shows the response of the sensors. Albeit the distance measurements are underestimated due to the reflectance of the opposite gripper (actually at a distance of around 4 cm) and the airplane wing, the presence of the airplane wing is clearly discernible. As the wing starts appearing in the field of view of the sensors we see a steep decrease in distance, which then reaches a minimum at the wing's center, and then gradually increases as the robot arm moves away from the wing. This is due to the fact that the infrared emitter is better approximated by a lobe than by a ray. The symmetry of the reflected plane at the center of the wing causes the photo receiver to receive the maximum possible reflected intensity available from the airplane wing, illustrating the limitations in lateral resolution, which would need to be compensated by an orthogonal sweep, should a more accurate 3D reconstruction be desired.

We have also explored contact sensing, which is not affected by surface reflectivity, to construct simple 3D models. Figure 16, left, shows a staircase from YCB wooden blocks (1 square inch). Figure 16, right, shows the resulting point cloud after manually moving the robot to make contact with his left finger (green points), its right finger (cyan points), and its left and right finger tip (violet and blue points). Figure 16, right, also shows data from an RGB-D sensor (Asus Xtion), whose calibration is slightly off. We note that the point cloud that we obtained using tactile sensing also contains data from the top and the back of the staircase, which are not available from the RGB-D camera.

5.5 Improving Camera Alignment

As camera calibration is a recurrent problem in robotics, we have also investigated whether tactile information can be used to correct calibration error of a RGB-D camera. In addition to calibrating the intrinsic non-linear parameters of a camera, camera calibration requires calculating a transformation to find the location of the objects from the camera's viewpoint to a location relative to the robot arm. To find the latter transformation, we rigidly mount an augmented reality (AR) tag to a known location on the robot wrist. Despite successful calibration of the intrinsic camera parameters, this kind of calibration usually leads to an error of around 3cm (Figure 17, middle) due to low resolution of the RGB-D data and use of only one AR Tag.

To mitigate the offset errors due to calibration we use contact sensing information in a feedback loop to find a more accurate transformation. We make the Baxter robot touch objects to obtain their correct physical location in space. The misalignment in the calibration is calculated based off the transformation between known

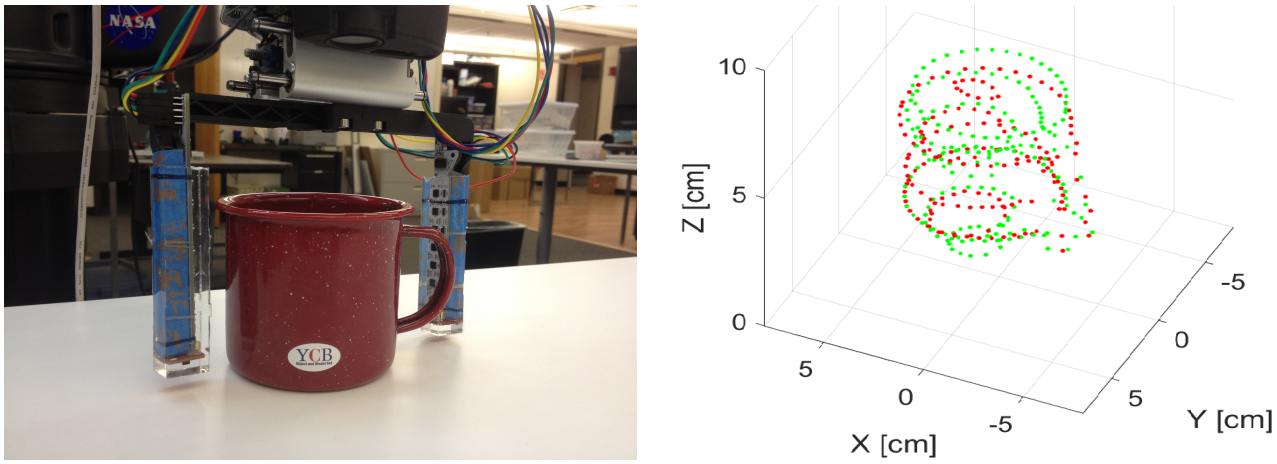

Fig. 14: Left: Scanning the YCB cup by performing a 360 degree swivel. Right: 3D point cloud model of a cup rendered from proximity measurements. The red colored points are from the left finger sensor and the green colored points from the right finger sensor.

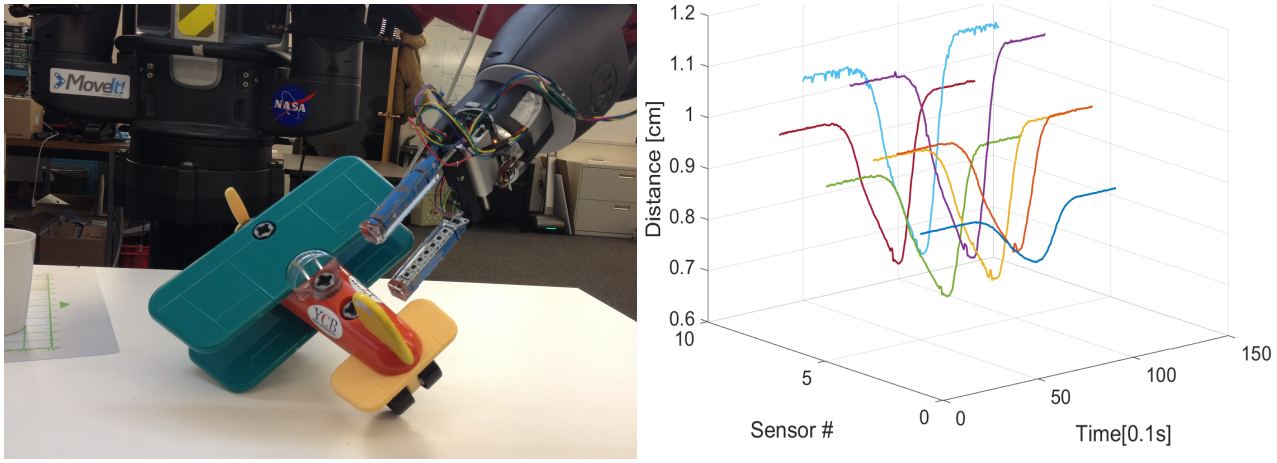

Fig. 15: Left: Scanning the wing of a toy airplane from the YCB object set using the custom designed Baxter grippers. Right: Recorded proximity measurements from horizontal sweep across airplane wing, only data from the right finger is shown.

physical location of the object and the location of the object as perceived by the camera. An example of this is shown in Figure 17. Using the Baxter grippers, we search for wooden cubes on a table. Due to the expected 3cm offset error, a radius of 3cm around each block's centroid was searched until the internal finger sensors detected contact. The blue and violet spheres show the finger tips' scanning trajectory over the table. When the left finger sensors reported internal contact (shown as the cyan spheres), the grippers scanned along the sides of the block, the green spheres showing contact from the right finger sensors that were used to scan the other side of the block. Scanning allows us to find the four corners of the block and calculate the true centroid. We performed this for all four cubes using both tactile information and RGB-D data and then calculated the transformation between the two sets of points, which is a simple optimization problem. The result is shown in Figure 17, right, demonstrating close alignment between tactile and RGB-D information.

6 Discussion

The proposed sensor has a series of design parameters, ranging from the choice of the material itself, its mixing ratio, its thickness, and the current at which the emitter operates. Each of these parameters affects the sensors' range, dynamic range, and thereby resolution and accuracy. While far from exhaustive, systematic experiments presented here highlight important trends, and allow to obtain a good trade-off between ranging and

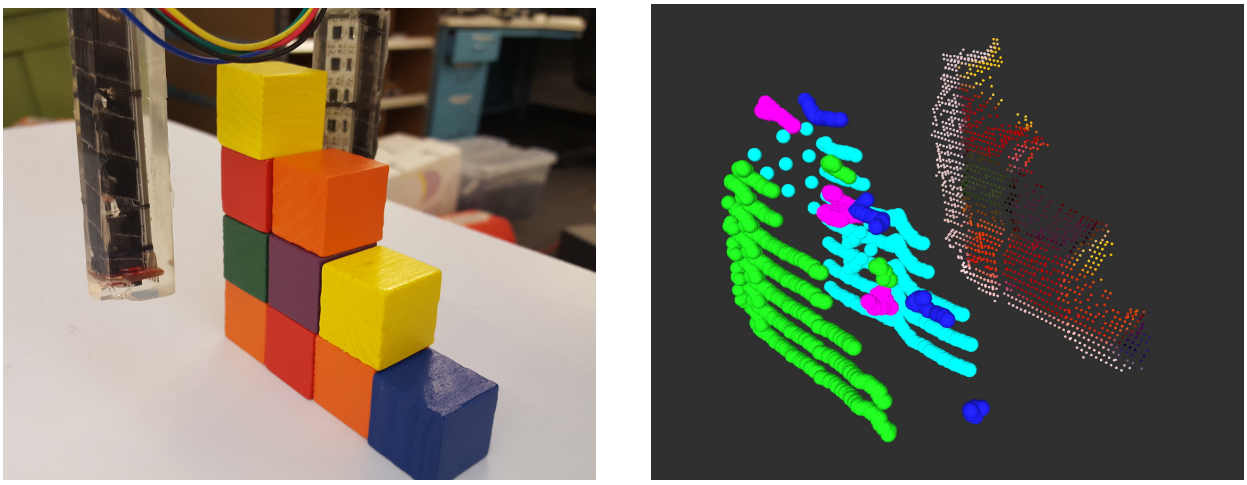

Fig. 16: Left: Using the custom made Baxter gripper to scan a staircase of blocks using touch sensing (manual operation), we were able to produce the brightly colored point cloud in the right image. Right: Comparison of a point cloud obtained via tactile sensing and data from a RGB-D sensor (Asus Xtion). RGB-D data is offset due to calibration error.

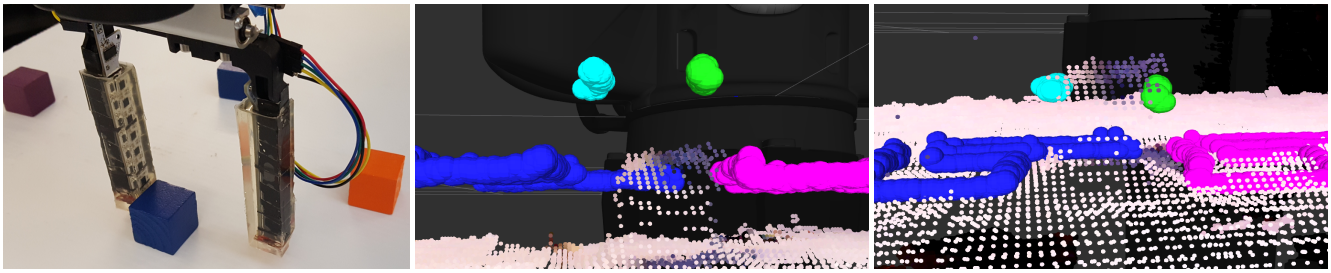

Fig. 17: Left: Using the tactile sensors on the Baxter gripper, we searched and scanned for four blocks on a table. Middle: Colored spheres display where the sensors reported contact compared to where the point cloud shows the cube and table to be located. Bottom right: The same point cloud and contact points after aligning touch and depth information. Green and cyan spheres are contact from the inside of the gripper's fingers, and the violet and blue spheres show contact at the fingertips.

force sensing capabilities, as well as providing guidelines on how to adapt the sensor to one's own specifications.

Albeit roughly following the form $y = ax^b + c$, our approximation introduces non-negligible systematic error, an effect that gets amplified by adding a PDMS layer, which introduces another constant to the denominator of (2). While better non-linear approximations could be found, e.g., using support vector machines or training a neural network, the sensor is very sensitive to surface properties. For example, black paper is five times less reflecting than white paper, whereas shiny objects are more reflecting than objects with rougher surfaces. We observe, however, that most practical application of the proposed sensor might not require calibration at all. Indeed, centering around an object only requires equalizing raw sensor readings, which are both monotonically increasing and continuous from infinite distance to at least $5N$ force.

We also observe that the shape of the function that relates distance/force measurements to raw sensor readings is of similar quality independent of the surface properties, thickness, mixing ratio, and current, with an inflection point at the contact point. Performing a firm grasp on an unknown object such as the panhandle in Figure 12 allows to record such a curve in its entirety and might allow to infer its material properties given all other parameters of the sensor are known. For example, when squeezing the handle, the sensor reading maxes out at around 2.1×10^4, which is slightly above the value of black paper at 120mA (1.8×10^4) for 6mm PDMS (8:1). Together with actual distance information obtained from the gripper itself, it might be possible to calibrate the sensor online by performing a simple grasp, and then use this data to perform an accurate 3D reconstruction. Squeezing an object might also provide insight for tuning the sensing current. For example, the sensor current could be reduced until the sensor saturates at a value below the maximum reading, and calibration data could be obtained during a second squeeze. Finally, tactile and geometry information could complement existing approaches in which robots

use active manipulation to understand objects in their environment (Oberlin and Tellex, 2015; Ma et al, 2015).

Another limitation of optical proximity sensors is their dependence on the angle of incidence. While this is not noticed with rotation symmetric objects such as those used here, scanning a rectangular object using a circular swivel motion, e.g., would let the object appear elliptically. As the resulting error is well quantified (Benet et al, 2002), we wish to investigate how contact information can be exploited to estimate the angle of a surface, and investigate sensor-based motion planning techniques that can help the robot to differentiate between accurate and erroneous signals by automatically testing different hypothesis of the true object's pose and surface properties.

Due to the sensitivity of the sensor to surface reflectivity and surface angle, the current 3D models from proximity measurements are currently too noisy to rely on solely for 3D reconstruction. This is not the case when obtaining data points from actual manipulation of the object. In future work, we wish to explore how to combine this data. For example, once contact has been made, one could re-compute all incidence points that have been gathered before touch. In addition to contact data itself, previous positions and speed of the robot might help to improve the estimation of surface properties, whereas multiple contact points can be used to estimate surface angle. Data collected in such a way would not only allow to complement RGB-D data, but might replace such a sensor altogether, for example when operating in narrow passage ways such as inside a drawer or a shelf.

Indeed, experiments with wooden blocks of different colors demonstrate that contact sensing is indeed little sensitive to surface reflectivity and can be accomplished without exerting force onto the object. This is important, as force-based contact sensing possibly alters the position of an object, making it difficult to obtain a consistent 3D model or perform reliable manipulation.

Summarizing the various applications of PCF-sensing in robotic manipulation suggests a hierarchy of sensing modalities: Proximity data can help during the approach phase before contact is made. Contact sensing can then be exploited to impose constraints on an object before any forces that possibly move the object are exerted. Force sensing, finally, can then be used to control the grasp in the spirit of Fearing (1986).

7 Conclusion and further work

We present an integrated proximity, contact and force sensor that is simple to manufacture and low-cost, yet provides a series of benefits that usually require much more complex sensors. We experimentally evaluate the design space and demonstrate the impact of different material properties and control parameters on the sensor response. As expected with infrared-based sensors, the sensor is strongly non-linear, highly sensitive to surface properties and has poor lateral resolution when compared with ray-based or RGB-D sensors. Nevertheless, we demonstrate that the proposed sensor has a wide range of use cases that facilitate grasping and manipulation ranging from contact point detection, determining grasp points, to object registration. In the future we wish to investigate better sensor models and sensor-based motion planning strategies such as squeezing and scanning an object. In the long run, the necessary processing could be co-located with the sensor, literally creating materials that make robots smart.

Acknowledgements This research was supported by the Airforce Office of Scientific Research. We are grateful for this support.

References

Ando S, Shinoda H (1995) Ultrasonic emission tactile sensing. IEEE Control Systems Magazine 15(1):61–69

Armani D, Liu C, Aluru N (1999) Re-configurable fluid circuits by PDMS elastomer micromachining. In: Micro Electro Mechanical Systems, 1999. MEMS'99. Twelfth IEEE International Conference on, IEEE, pp 222–227

Balek D, Kelley R (1985) Using gripper mounted infrared proximity sensors for robot feedback control. In: Robotics and Automation. Proceedings. 1985 IEEE International Conference on, IEEE, vol 2, pp 282–287

Benet G, Blanes F, Simó JE, Pérez P (2002) Using infrared sensors for distance measurement in mobile robots. Robotics and Autonomous systems 40(4):255–266

Bohg J, Morales A, Asfour T, Kragic D (2014) Data-driven grasp synthesis—a survey. Robotics, IEEE Transactions on 30(2):289–309

Born M, Wolf E (1999) Principles of optics: electromagnetic theory of propagation, interference and diffraction of light. Cambridge University press

Cai D, Neyer A, Kuckuk R, Heise HM (2010) Raman, mid-infrared, near-infrared and ultraviolet–visible spectroscopy of pdms silicone rubber for characterization of polymer optical waveguide materials. Journal of Molecular Structure 976(1):274–281

Cai Z, Qiu W, Shao G, Wang W (2013) A new fabrication method for all-PDMS waveguides. Sensors and Actuators A: Physical 204:44–47

Calli B, Walsman A, Singh A, Srinivasa S, Abbeel P, Dollar AM (2015) Benchmarking in manipulation research: The YCB object and model set and benchmarking protocols. arXiv preprint arXiv:150203143

Chen K, Wo A, Chen Y (2006) Transmission spectrum of PDMS in 4-7μm mid-IR range for characterization of protein structure. In: NSTI-Nanotech, vol 2, pp 732–735

Chossat JB, Park YL, Wood RJ, Duchaine V (2013) A soft strain sensor based on ionic and metal liquids. IEEE Sensors Journal 13(9):3405–3414

Correll N, Bekris KE, Berenson D, Brock O, Causo A, Hauser K, Okada K, Rodriguez A, Romano JM, Wurman PR (2016) Analysis and observations from the first amazon picking challenge. IEEE Transactions on Automation Science and Engineering

Cox R, Correll N (2017) Merging local and global 3d perception using contact sensing. In: AAAI Spring Symposium on Interactive Multi-Sensory Object Perception for Embodied Agents, Stanford, CA

Dafle NC, Rodriguez A, Paolini R, Tang B, Srinivasa SS, Erdmann M, Mason MT, Lundberg I, Staab H, Fuhlbrigge T (2014) Extrinsic dexterity: In-hand manipulation with external forces. In: Robotics and Automation (ICRA), 2014 IEEE International Conference on, IEEE, pp 1578–1585

Dahiya RS, Metta G, Valle M, Sandini G (2010) Tactile sensing: from humans to humanoids. Robotics, IEEE Transactions on 26(1):1–20

Dahiya RS, Mittendorfer P, Valle M, Cheng G, Lumelsky VJ (2013) Directions toward effective utilization of tactile skin: A review. Sensors Journal, IEEE 13(11):4121–4138

Deimel R, Brock O (2014) A novel type of compliant, underactuated robotic hand for dexterous grasping. Robotics: Science and Systems, Berkeley, CA pp 1687–1692

Dollar AM, Jentoft LP, Gao JH, Howe RD (2010) Contact sensing and grasping performance of compliant hands. Autonomous Robots 28(1):65–75

Farrow N, Correll N (2015) A soft pneumatic actuator that can sense grasp and touch. In: Intelligent Robots and Systems (IROS), 2015 IEEE/RSJ International Conference on, IEEE, pp 2317–2323

Farrow N, Li Y, Correll N (2016) Morphological and embedded computation in a self-contained soft robotic hand. arxiv:160500354

Farrow N, McIntire L, Correll N (2017) Functionalized textiles for interactive soft robotics. In: Int. Conf. on Robotics and Automation (ICRA)

Fearing R (1986) Simplified grasping and manipulation with dextrous robot hands. IEEE Journal on Robotics and Automation 2(4):188–195

Fujimori Y, Ohmura Y, Harada T, Kuniyoshi Y (2009) Wearable motion capture suit with full-body tactile sensors. In: Robotics and Automation, 2009. ICRA'09. IEEE International Conference on, IEEE, pp 3186–3193

Goger D, Alagi H, Wörn H (2013) Tactile proximity sensors for robotic applications. In: Industrial Technology (ICIT), 2013 IEEE International Conference on, IEEE, pp 978–983

Gray BL, Fearing RS (1996) A surface micromachined microtactile sensor array. In: Robotics and Automation, 1996. Proceedings., 1996 IEEE International Conference on, IEEE, vol 1, pp 1–6

Hellard G, Russell RA (2002) A robust, sensitive and economical tactile sensor for a robotic manipulator. In: Australian Conference on Robotics and Automation, Citeseer, pp 100–104

Hsiao K, Nangeroni P, Huber M, Saxena A, Ng AY (2009) Reactive grasping using optical proximity sensors. In: Robotics and Automation, 2009. ICRA'09. IEEE International Conference on, IEEE, pp 2098–2105

Hughes D, Correll N (2015) Texture recognition and localization in amorphous robotic skin. Bioinspiration & biomimetics 10(5):055,002

Jiang L, Low K, Costa J, Black RJ, Park YL (2015) Fiber optically sensorized multi-fingered robotic hand. In: Intelligent Robots and Systems (IROS), 2015 IEEE/RSJ International Conference on, IEEE, pp 1763–1768

Konstantinova J, Stilli A, Althoefer K (2015) Force and proximity fingertip sensor to enhance grasping perception. In: Intelligent Robots and Systems (IROS), 2015 IEEE/RSJ International Conference on, IEEE, pp 2118–2123

Kröger T, Finkemeyer B, Winkelbach S, Eble LO, Molkenstruck S, Wahl FM (2008) A manipulator plays Jenga. Robotics & Automation Magazine, IEEE 15(3):79–84

Lancaster S (2004) A fuzzy logic controller for the application of skin pressure. In: Fuzzy Information, 2004. Processing NAFIPS '04. IEEE Annual Meeting of the, vol 2, pp 686–689 Vol.2, DOI 10.1109/NAFIPS.2004.1337384

Lee HK, Chung J, Chang SI, Yoon E (2008) Normal and shear force measurement using a flexible polymer tactile sensor with embedded multiple capacitors. Microelectromechanical Systems, Journal of 17(4):934–942

Ma L, Ghafarianzadeh M, Coleman D, Correll N, Sibley G (2015) Simultaneous localization, mapping, and

manipulation for unsupervised object discovery. In: IEEE International Conference on Robotics and Automation, pp 1344–1351

Maldonado A, Alvarez H, Beetz M (2012) Improving robot manipulation through fingertip perception. In: Intelligent Robots and Systems (IROS), 2012 IEEE/RSJ International Conference on, IEEE, pp 2947–2954

Mittendorfer P, Cheng G (2011) Humanoid multimodal tactile-sensing modules. Robotics, IEEE Transactions on 27(3):401–410

Mittendorfer P, Yoshida E, Cheng G (2015) Realizing whole-body tactile interactions with a self-organizing, multi-modal artificial skin on a humanoid robot. Advanced Robotics 29(1):51–67

Nakamura K, Shinoda H (2001) A tactile sensor instantaneously evaluating friction coefficients. In: Transducers 01 Eurosensors XV, Springer, pp 1402–1405

Oberlin J, Tellex S (2015) Learning to pick up objects through active exploration. In: Development and Learning and Epigenetic Robotics (ICDL-EpiRob), 2015 Joint IEEE International Conference on, IEEE, pp 252–253

Ohmura Y, Kuniyoshi Y, Nagakubo A (2006) Conformable and scalable tactile sensor skin for curved surfaces. In: Robotics and Automation, 2006. ICRA 2006. Proceedings 2006 IEEE International Conference on, IEEE, pp 1348–1353

Patel R, Correll N (2016) Integrated force and distance sensing using elastomer-embedded commodity proximity sensors. In: Proceedings of Robotics: Science and Systems

Patel R, Canardo Alastuey J, Correll N (2016) Improving grasp performance using in-hand proximity and force sensing. In: Int. Symposium on Experimental Robotics (ISER), Tokyo, Japan

Patel R, Cox R, Romero B, Correll N (2017) Improving grasp performance using in-hand proximity and contact sensing. arXiv preprint arXiv:170106071

Romano JM, Hsiao K, Niemeyer G, Chitta S, Kuchenbecker KJ (2011) Human-inspired robotic grasp control with tactile sensing. IEEE Transactions on Robotics 27(6):1067–1079

Rossiter J, Mukai T (2006) An led-based tactile sensor for multi-sensing over large areas. In: Sensors, 2006. 5th IEEE Conference on, IEEE, pp 835–838

Tenzer Y, Jentoft LP, Howe RD (2014) The feel of mems barometers: inexpensive and easily customized tactile array sensors. Robotics & Automation Magazine, IEEE 21(3):89–95

Wang L, Beebe DJ (2002) Characterization of a silicon-based shear-force sensor on human subjects. Biomedical Engineering, IEEE Transactions on 49(11):1340–1347

Zhang ZF, Tao XM, Zhang HP, Zhu B (2013) Soft fiber optic sensors for precision measurement of shear stress and pressure. Sensors Journal, IEEE 13(5):1478–1482

Zhu F, Spronck J (1992) A capacitive tactile sensor for shear and normal force measurements. Sensors and Actuators A: Physical 31(1):115–120